Nanoelectronics and Its New Materials – A NEW ERA OF NANOSCIENCE

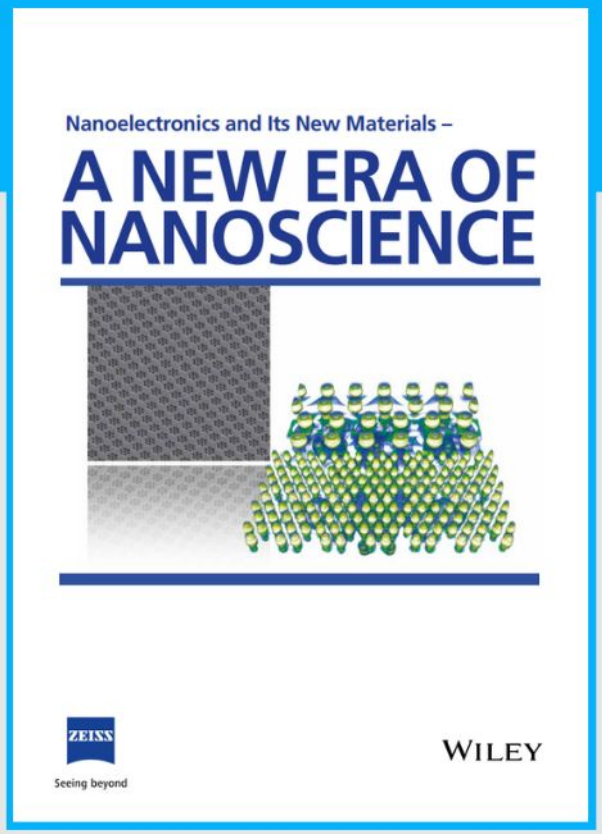

Discover the recent advances in electronics research and fundamental nanoscience.

Nanotechnology has become the driving force behind breakthroughs in engineering, materials science, physics, chemistry, and biological sciences. In this compendium, we delve into a wide range of novel applications that highlight recent advances in electronics research and fundamental nanoscience. From surface analysis and defect detection to tailored optical functionality and transparent nanowire electrodes, this eBook covers key topics that will revolutionize the future of electronics.

To get your hands on this valuable resource and unleash the power of nanotechnology, simply download the eBook now. Stay ahead of the curve and embrace the future of electronics with nanoscience as your guide.

ZEISS

Seeing beyond

WILEY

ADVANCED FUNCTIONAL MATERIALS
www.afm-journal.de

$CsPbBr_3$@Glass Nanocomposite with Green-Emitting External Quantum Efficiency of 75% for Backlit Display

*Shuxin Chen, Jidong Lin, Jie Huang, Tao Pang, Qingying Ye, Yuanhui Zheng, Xiaoyan Li, Yunlong Yu, Bin Zhuang, and Daqin Chen**

Robust amorphous glass protected $CsPbBr_3$ ($CsPbBr_3$@glass) perovskite quantum dots (PeQDs) with ultra-pure green emission and superior long-term stability are highly desirable for developing wide-color-gamut liquid crystal displays. However, most of the reported $CsPbBr_3$@glass nanocomposites are subject to low external quantum efficiency (EQE). This work demonstrates that ZrO_2 additive has an "accumulation" effect on the borosilicate glass network structure to promote in situ nucleation/growth of PeQDs inside glass rather than self-crystallization. This effect is beneficial in reducing surface defects, improving the quality of PeQDs, and thus boosting radiative recombination of excitons. As a consequence, the as-prepared $CsPbBr_3$@glass shows a record EQE of up to 75% and can pass the accelerated aging tests at 85 °C/85% RH for 1000 h and blue light irradiation over 2000 h. Finally, a prototype display using $CsPbBr_3$@glass-based straight-down backlit unit is designed and gains more favorable responses in blind selection tests for its high brightness of 2647 cd m^{-2} and high color purity of 88%. The findings will pave the way for realizing the commercial application of $CsPbBr_3$@glass nanocomposite in PeQDs-converted backlit display.

1. Introduction

Currently, liquid crystal display (LCD), the dominant display technology used in information terminals, has formed a mature scale production through the regulation of light output in the liquid crystal layer and the optimization of light-emitting diode (LED) backlight. In the pursuit of higher-quality backlit displays, the most intuitive indicators affecting human feeling are color gamut and brightness, which measure the reproduction ability of object color and light output luminance, respectively.[1] The full width at half maximum (fwhm) of a luminescent material determines its color purity and higher color purity produces a wider color gamut.[2] Current commercial white LED (wLED) backlight consists of a blue chip and a broadband yellow phosphor (YAG:Ce^{3+}).[3] Such white light passing through the color filter causes much yellow light to be filtered, leading to a low color gamut of ≈72% NTSC and failing to make energy savings.[4] In addition, increasing the light output brightness of LCD usually results in increased power consumption. Therefore, achieving a balance between color/brightness and power consumption of LCD falls to the improvement of the backlit module.

Lead halide perovskite quantum dots (PeQDs) have been used in backlit displays due to their visible full spectral tunability, high luminescence quantum efficiency (QE), and large absorption

S. Chen, J. Lin, J. Huang, Q. Ye, B. Zhuang, D. Chen
College of Physics and Energy
Fujian Normal University
Fuzhou, Fujian 350117, P. R. China
E-mail: dqchen@fjnu.edu.cn

T. Pang
Huzhou Key Laboratory of Materials for Energy Conversion and Storage
College of Science
Huzhou University
Huzhou, Zhejiang 313000, P. R. China

Y. Zheng, D. Chen
Fujian Science & Technology Innovation Laboratory for Optoelectronic Information
Fuzhou, Fujian 350116, P. R. China

Y. Zheng
College of Chemistry
Fuzhou University
Fuzhou, Fujian 350116, P. R. China

X. Li, Y. Yu
Organic Optoelectronics Engineering Research Center of Fujian's Universities
College of Electronics and Information Science
Fujian Jiangxia University
Fuzhou 350108, P. R. China

D. Chen
Fujian Provincial Collaborative Innovation Center for Advanced High-Field Superconducting Materials and Engineering
Fuzhou, Fujian 350117, P. R. China

D. Chen
Fujian Provincial Engineering Technology Research Center of Solar Energy Conversion and Energy Storage
Fuzhou, Fujian 350117, P. R. China

The ORCID identification number(s) for the author(s) of this article can be found under https://doi.org/10.1002/adfm.202309293

DOI: 10.1002/adfm.202309293

cross-section.[5–10] Especially, all inorganic $CsPbX_3$ (X = Br and Br/I) PeQDs are able to provide finely tunable green emissions (525–535 nm) and red ones (630–640 nm) with high color purity, which guarantees a wide color gamut display.[11–13] The white light spectrum of the backlight made up of PeQDs largely coincides with the spectral range of the color filter, thus significantly improving backlight utilization. PeQDs-based backlight can enhance the color quality of LCD with improved perceived brightness due to the well-known Helmholtz–Kohlrausch effect.[14–16] Unfortunately, naked PeQDs suffer from long-term instability of their ionic crystal nature, which prevents them from passing through commercial aging standards at 85 °C/85%RH and blue-light-irradiation stability. Among several reported strategies, in situ nucleation/growth of PeQDs inside a robust inorganic glass network (denoted as PeQDs@glass) has been demonstrated to be practicable for the effective isolation of PeQDs from the external environment.[17–28] Generally, the brightness of PeQDs is previously believed to be associated with internal QE (IQE), defined as the ratio of the number of output photons to the number of absorbed ones. However, for practical display applications, high-power blue light is input for photoexcitation. Therefore, it is more feasible to adopt external QE (EQE) to characterize PeQDs@glass, which is defined as the ratio of the number of output photons to the number of incident ones. As a consequence, PeQDs@glass with strong absorbance and low non-radiative relaxation probability is highly desirable, but the related topic remains unexplored.

Herein, ZrO_2 additive is used to modulate B_2O_3-SiO_2-based glass network structure and control $CsPbBr_3$ crystallization and optical properties. The introduction of an appropriate amount of Zr^{4+} ions is demonstrated to have an "accumulation" effect on the glass network, which inhibits the self-crystallization of PeQDs inside glass and promotes their in situ nucleation/growth, which is conducive to the reduction of defects and the improvement of the quality of PeQDs. The as-prepared $CsPbBr_3$@glass yields ultrapure green light emission at 527 nm with a high color purity of 88% and a record-high EQE of 75%. The highest luminance of 2647 cd m^{-2} is achieved for the $CsPbBr_3$@glass optical film under 450 nm blue light (375 cd m^{-2}) excitation. And the $CsPbBr_3$@glass exhibits excellent long-term stability and meets commercial aging standard at 85 °C/85% RH for 1000 h and blue light irradiation (optical power: 40 W m^{-2}) for 2200 h. Finally, straight down prototype display based on PeQDs@glass wLED array backlit module is designed and receives more favorable responses in blind selection tests for its wide color gamut (118% NTSC standard).

2. Results and Discussion

A series of borosilicate glasses with fixed perovskite components and varied amounts of ZrO_2 (Table S1, Supporting Information) are prepared by a melt quenching method and the CsPbBr3@glass nanocomposites are realized via in situ glass crystallization at 520 °C for 4 h (Figure S1, Supporting Information). X-ray photoelectron spectroscopy (XPS) and energy dispersive X-ray (EDX) data confirm the presence of all glass and perovskite elements within the fabricated samples (Figures S2 and S3, Supporting Information). As illustrated in **Figure 1**a, the addition of ZrO_2 has a remarkable effect on the appearance of precursor glasses (PGs), which shows a gradual conversion from transparent yellow glass with PeQDs self-crystallization into opacified glass with the precipitation of ZrO_2 crystals (Figure S4, Supporting Information). The glass with 6 mol% ZrO_2 is completely transparent and no green emitting is observed under UV light excitation, confirming that the appropriate ZrO_2 additive can inhibit self-crystallization of $CsPbBr_3$ PeQDs inside the glass. As shown in Figure 1b, typical cubic $CsPbBr_3$ crystalline diffraction peaks are superimposed on the amorphous halo for all the samples after heat-treatment, and extra diffraction peaks of monoclinic ZrO_2 crystal are detected in the 8 mol% ZrO_2 added sample. Transmission electron microscope (TEM) images verify that $CsPbBr_3$ PeQDs with sizes of 10–15 nm are well discerned inside the glass matrix (Figure 1c; Figure S5, Supporting Information). High-resolution TEM (HRTEM) micrograph evidences high crystallinity of $CsPbBr_3$ particles with distinct interplanar spacing of 0.319 nm corresponding to (111) plane (Figure 1d).

Fourier transform infrared (FTIR) spectra reveal the variation of vibrational structure of B–O and Si–O in the glass network caused by ZrO_2 additive, as depicted in **Figure 2**a. Enhanced signals for B–O–B bending vibration at 650–750 cm^{-1}, B–O stretching vibration in the $[BO_3]$ triangle at 1300–1550 cm^{-1}, bending vibration of the Si–O–Si bond in the $[SiO_4]$ tetrahedral unit and stretching vibration of the $[BO_4]$ unit at 1000–1100 cm^{-1} are observed in samples containing ZrO_2.[29–31] Raman spectra show strong characteristic peak of $CsPbBr_3$ at 20–80 cm^{-1} belonging to the second-order phonon mode of the $[PbBr_6]^{4-}$ octahedron, further confirming the successful precipitation of $CsPbBr_3$ in glass (Figure 2b). Concurrently, a vibrational peak attributed to Si–O–B at 1200–1400 cm^{-1} appears to increase and then weakens with an increase in ZrO_2 content.[32] In addition, Raman signals of ZrO_2 crystals are detected in the 8 mol% ZrO_2 added sample.[33] To verify the altered glass network structure, we further investigated magic angle spinning nuclear magnetic resonance (MAS-NMR) spectra of ^{29}Si and ^{11}B (Figure 2c,d). ^{29}Si NMR spectra exhibit a broadband feature owing to the wide distribution of Q^n units (quaternary silicon, n = 2–4). Each spectrum can be deconvoluted into three peaks ≈−88.5, −92, and −100 ppm using the Gaussian peak shape function. Due to BO_4-BO_4 links being thought to be low probability for the relatively high charge on $^{[4]}B$–O–$^{[4]}B$, ^{11}B MAS spectra have been deconvoluted into three peaks ($^{[3]}B$(ring), $^{[3]}B$(nonring), and $^{[4]}B$(1B,3Si)).[34–36] The corresponding NMR decomposition results and relative percentages of each species are tabulated in **Table 1**. With the increase of ZrO_2 concentration, the contents of Q^2 and Q^3 decrease, but that of Q^4 significantly enhances. On the contrary, the proportion of $[BO_4]$ (1B,3Si) drops, and the proportions of BO_3 ring and BO_3 non-ring rise. These results indicate that the high bond strength and ionic potential of Zr^{4+} ions in glass enhance the network connectivity of $[SiO_4]$ by the partial conversion of $[BO_4]$ to $[BO_3]$ with the release of free oxygen. Excessive ZrO_2 provides large amounts of Zr^{4+} ions, which start to capture the oxygen ions to form $[ZrO6]^{2-}$.[37] This leads to the participation of ZrO_2 crystals in the glass network structure and makes the glass opaque.

In support of this view, high-resolution XPS data of Si 2*p*, O 1*s*, and Zr 3*d* for the 0, 6, and 8 mol% ZrO_2 added samples are shown in Figure S6 (Supporting Information). The Si 2*p* signal deconvoluted into three components at 101.3, 102.2, and 103.2 eV is attributed to Si bonding in Q^2, Q^3, and Q^4 units, respectively,

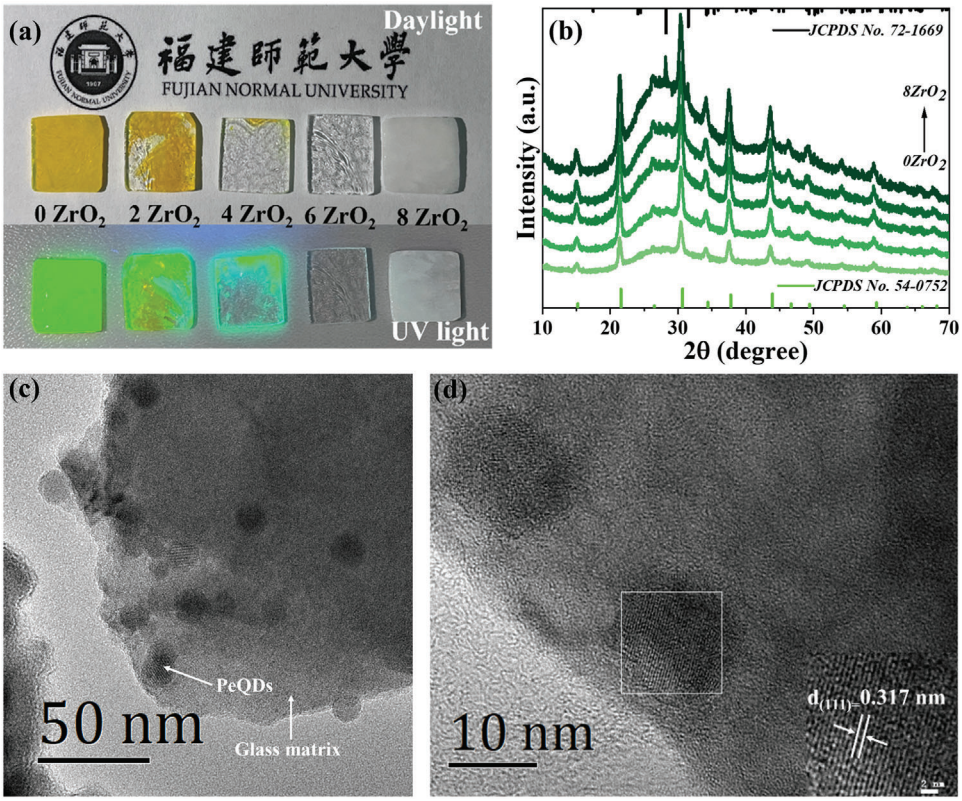

Figure 1. a) Digital photographs of the precursor glasses under daylight and UV lamp excitation. b) XRD patterns of $CsPbBr_3$@glass with the addition of different amounts of ZrO_2. Bars in (b) represent standard diffraction data of cubic $CsPbBr_3$ crystal (JCPDS No. 54-0752) and monoclinic ZrO_2 crystal (JCPDS No. 72-1669). c) TEM and d) HRTEM images of a typical $CsPbBr_3$@glass sample.

which also shows a tendency of enhancement of Q^4 unit with the increase of ZrO_2 concentration. The O 1s signal deconvoluted into two components at 530.8 and 532.0 eV corresponds to Si–O–Zr and Si–O–Si, respectively.[38,39] Obvious doublets of the Zr 3*d* signal at 182.5 and 185.0 eV are assigned to the binding energies of Zr $3d_{5/2}$ and Zr $3d_{3/2}$, and the XPS signal at 182.5 eV originated from Si–O–Zr bond.[40–43] Therefore, it can be concluded that the Zr^{4+} species are in the silica framework rather than bulk ZrO_2. Accordingly, we summarize the variation of the glass network structure upon the addition of ZrO_2, as schematically illustrated in Figure 2e and Figure S7 (Supporting Information). The introduced ZrO_2 is present in the borosilicate glass system as an intermediate oxide. As the Zr^{4+} content gradually increases, the "accumulation" effect on the surrounding [SiO_4] becomes more and more obvious benefited from its intrinsic high bond strength, high coordination, and high ionic potential. This action not only captures the free oxygen from its own surroundings, but also robs O^{2-} from [BO_4], resulting in a decrease in the amount of [BO_4] and an increase in the amount of [BO_3]. Simultaneously, another conversion of Q^2 & Q^3 into Q^4 of [SiO_4] in the form of Si–O–Zr leads to an increase in the degree of polymerization of the glass network structure. The macroscopic manifestation is the gradual transition of precursor glass from a self-crystallization state to a transparent glass state. Ultimately, when the glass contains excess ZrO_2, the Zr^{4+} ions form a six-ligand structure within the glass network, causing the precursor glass to devitrification with the precipitation of ZrO_4 crystals.

Table 1. The decomposition data form the ^{29}Si and ^{11}B NMR spectra. δ_{iso} represents chemical shift. Q^n denotes quaternary silicon, where the superscript n = 2–4 indicates the number of bridging oxygens. ^3B and $^3B_{non}$ are defined as the triangle BO_3 group forming a ring or not, and ^4B represents the tetrahedral BO_4 group.

Elements	Species	δ_{iso}[ppm]	0-ZrO_2	6-ZrO_2	8-ZrO_2
			% area		
^{29}Si	Q^2	−88.5	47.6	34.8	25.1
	Q^3	−92.0	42.3	40.9	31.9
	Q^4	−100.0	10.1	24.3	43.0
^{11}B	^3B	12.8	10.9	13.3	17.4
	$^3B_{non}$	7.51	36.6	43.6	46.1
	^4B	0.40	52.5	43.1	36.5

The variation of glass structure will significantly affect in situ nucleation/growth of $CsPbBr_3$ PeQDs, leading to enhanced optical performance of $CsPbBr_3$@glass nanocomposites. As shown in **Figure 3**a, $CsPbBr_3$@glass samples with various ZrO_2 concentrations exhibit tunable green emissions within the sensitive spectral region for wide-color-gamut display. PL peak shows a blue-shift from 529 to 523 nm (inset of Figure 3a) and the fwhm value exhibits a slight decrease from 26.7 to 25.8 nm with increase of ZrO_2 concentration (Figure 3b), resulting in a high

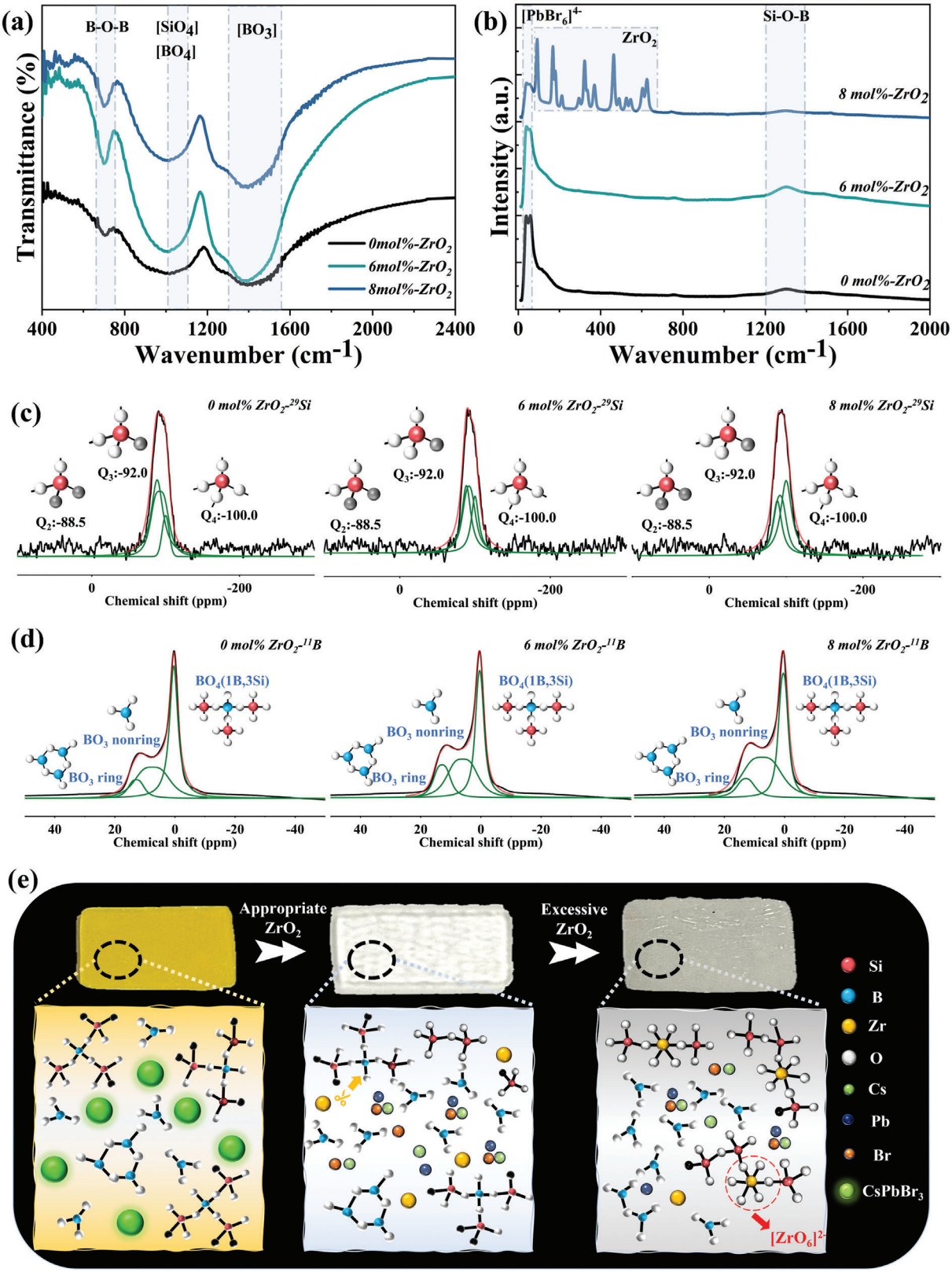

Figure 2. a) FTIR spectra, b) Raman spectra, c) ^{29}Si, and d) ^{11}B MAS-NMR spectra (black line) and the fitted results (red line: sum; green lines: components) for the $CsPbBr_3$@glass with different ZrO_2 concentrations. e) Schematic illustration of the influence of ZrO_2 additive on the variation of SiO_2-B_2O_3 glass network structure.

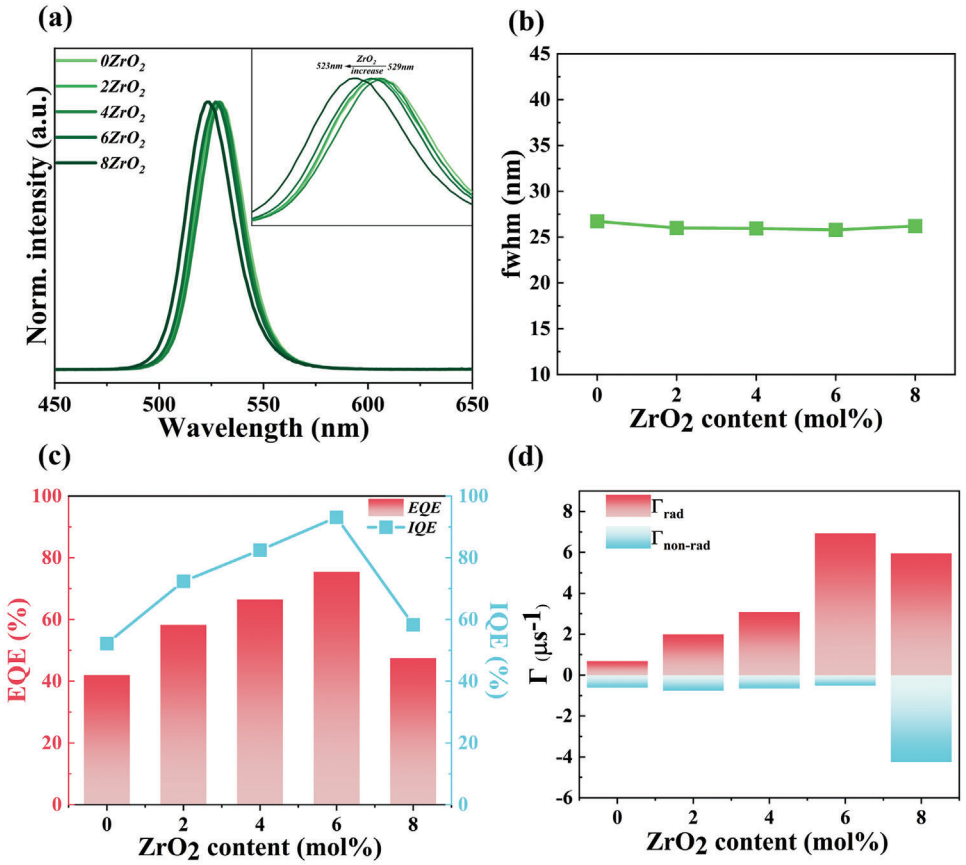

Figure 3. a) PL spectra, b) fwhm, c) EQE & IQE, and d) radiative and non-radiative rates for the $CsPbBr_3$@glass nanocomposites with different ZrO_2 concentrations.

color purity of ≈88%. This is attributed to ZrO_2-additive induced gradual increase in the degree of polymerization of the glass structure and confined growth of PeQDs inside glass, which leads to decreased size and improved uniformity of PeQDs. Furthermore, ZrO_2 concentration-dependent IQE and EQE are investigated (Table S2, Supporting Information). Generally, the increase in the IQE of the material tended to be achieved by reducing absorption, which may suffer from a noticeable brightness deficit when the material is put into application. To avoid this issue, we fabricated the composite materials with equal quantities of perovskite components in equal amounts of glass (Table S1, Supporting Information). As a consequence, all the samples were found to have the same high absorption efficiency of ≈80% (Figure S8 and Table S2, Supporting Information), eliminating the situation of high IQE with low absorption. Indeed, for the present case, both IQE and EQE values show a tendency of enhancement with increase of ZrO_2 concentration, and then decrease for the addition of excess 8 mol% ZrO_2 (Figure 3c). The IQE and EQE of the 6 mol% ZrO_2-added sample reach as high as 93% and 75%, respectively, which are the maximal values reported for the $CsPbBr_3$@glass samples so far (Table S3, Supporting Information).

Time-resolved photoluminescence (TRPL) was conducted to analyze the kinetics of exciton recombination, as shown in Figure S9 (Supporting Information). The decay of the fluorescence signals can be well-fitted via a tri-exponential function and the corresponding lifetimes of the three components are summarized in Table S4 (Supporting Information). It is found that the sample without the addition of ZrO_2 shows an average lifetime of 770 ns, much longer than the ZrO_2-added samples of 364, 267, 134, and 98 ns. Higher IQE and shorter decay lifetime indicate more efficient radiative recombination of excitons. Accordingly, the radiative recombination rate (Γ_{rad}) and non-radiative recombination rate ($\Gamma_{non\text{-}rad}$) of the $CsPbBr_3$@glass samples can be calculated with the following equations:

$$\Gamma_{rad} = \frac{\eta}{\tau_{ave}} \quad (1)$$

$$\Gamma_{non-rad} = \frac{1}{\tau_{ave}} - \Gamma_{rad} \quad (2)$$

where η and τ_{ave} represent IQE and average lifetime, respectively. The ZrO_2 concentration-dependent radiative and non-radiative recombination rates are plotted in Figure 3d. It is concluded that the 6 mol% ZrO_2 added sample has the highest radiative recombination rate and lowest non-radiative rate, corresponding to its highest IQE & EQE, that is, the best luminescence performance. The appropriate amount of ZrO_2 additive can inhibit the

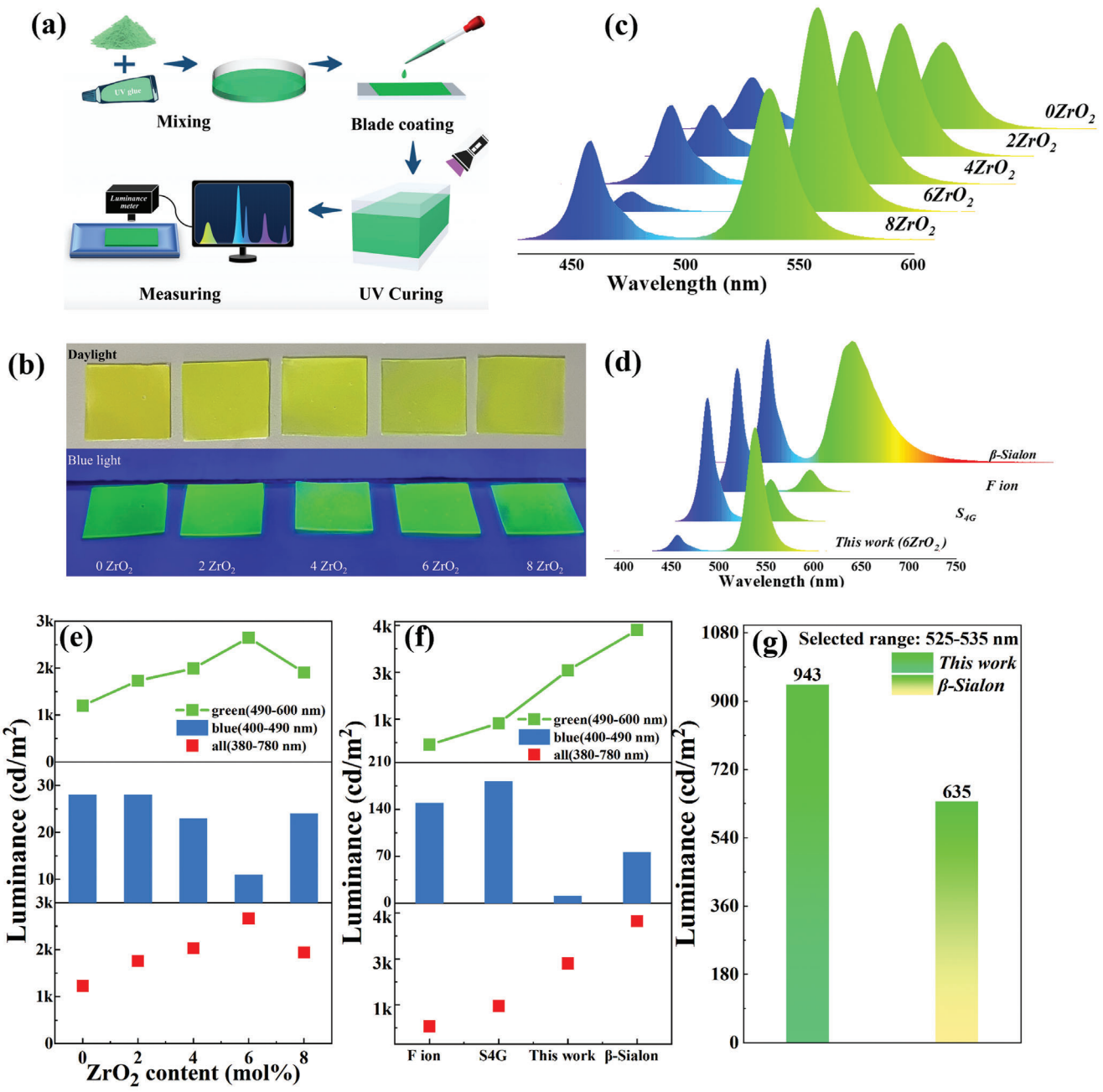

Figure 4. a) Schematical diagram of preparation procedure of $CsPbBr_3$@glass film for the brightness test. b) Photographs of the as-prepared films under daylight and blue light excitation. ZrO_2 concentration-dependent c) PL spectra and e) luminance for the green $CsPbBr_3$@glass films. Comparison of d) PL spectra and f) luminance for the present green film, previously reported films, and commercial β-Sialon film. g) Contrast plot of luminance between the 6-ZrO_2 $CsPbBr_3$@glass film and the β-Sialon film in the most eye-sensitive green emitting range from 525 to 535 nm.

self-crystallization of PeQDs in glass and promote the in situ growth of PeQDs, which is beneficial in reducing surface defects and improving the quality of PeQDs.

Further quantifying the emitting brightness (luminance) of $CsPbBr_3$@glass samples was performed with the help of a luminometer, as shown in **Figure 4**a. $CsPbBr_3$@glass was ground into powders and mixed evenly with UV-curable adhesive in a fixed weight ratio of 1:2, and $CsPbBr_3$@glass@UV-curable-glue is uniformly coated onto a double layer of transparent PET film and cured under a 365 nm UV lamp. All the as-prepared films yield intense green luminescence, and the film with 6 mol% ZrO_2 exhibits the brightest green light visible by the naked eye (Figure 4b). A blue light guide panel with a stable brightness of 375 cd m^{-2} and a startup time of 15 s was used as the test excitation light source (Figure S10, Supporting Information). As shown in Figure 4c,e, the radiance intensity gradually enhances and then weakens when ZrO_2 concentration goes beyond 6 mol%, which coincides with the variation tendency of IQE

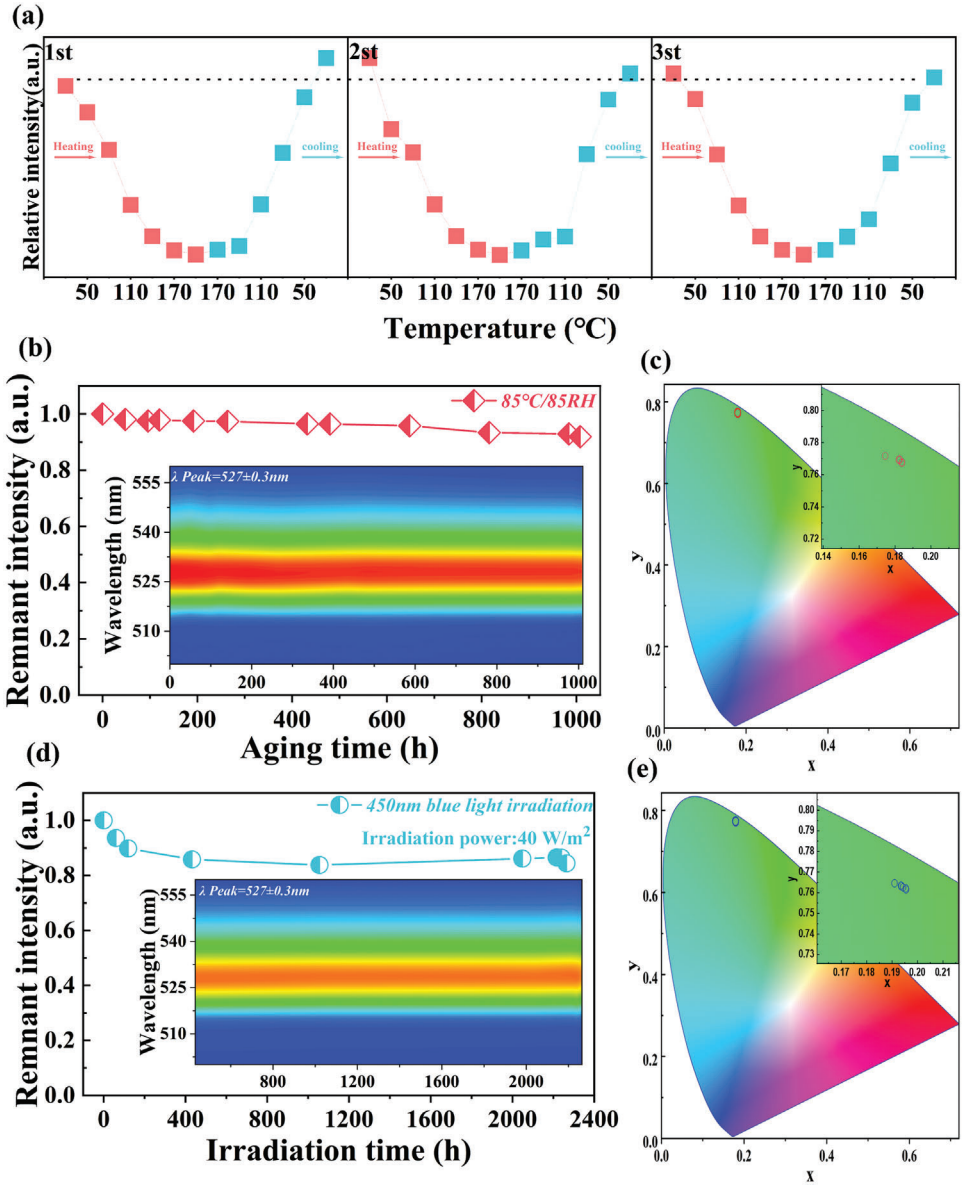

Figure 5. a) Relative PL intensity for the $CsPbBr_3$@glass sample experiencing three-time heating/cooling cycles between 20 and 200 °C. b) Heat/humidity resistance test of $CsPbBr_3$@glass under accelerated aging condition at 85 °C/85% RH. Inset is contour plot of PL spectra collected with elongation of aging duration. d) Photostability test under blue light (optical power: 40 W m^{-2}) irradiation. Inset is contour plot of PL spectra recorded with increase of irradiation duration. The alteration of CIE color coordinates of $CsPbBr_3$@glass over c) 85 °C/85% RH aging time and e) the blue light irradiation time.

& EQE (Figure 3c). We further divided the radiance spectrum (380–780 nm) into blue (400–490 nm) region and green (490–600 nm) one and calculated the corresponding luminance values. Apparently, the 6-ZrO_2 $CsPbBr_3$@glass film has a superior blue light absorption ability and exhibits excellent light conversion efficiency, whereby the maximal green light luminance can reach 2647 cd m^{-2} (Figure 4e). Compared to previously reported $CsPbBr_3$@glass composites, i.e., fluorine ion doped sample[44] only has brightness of 590 cd m^{-2} and S4G[45] one has a brightness of 1188 cd m^{-2} (Table S3, Supporting Information), the present material achieves a significant increase in green brightness (Figure 4d,f). Notably, commercial green powder (β-Sialon) has a higher brightness 3948 cd m^{-2}, however, this is mainly attributed to its broadband emission. Thus, we chose to compare the luminance in the green emitting range of 525–535 nm, which is the most eye-sensitive spectral region for wide-color-gamut display. As demonstrated in Figure 4g, the luminance of 6-ZrO_2 $CsPbBr_3$@glass film is much greater than that of commercial β-Sialon film.

We conducted a series of stability tests on a 6 mol% ZrO_2 $CsPbBr_3$@glass. As presented in Figure S11 (Supporting Information), PL intensity of $CsPbBr_3$@glass sample decreases with an elevation of temperature owing to intrinsic thermal quenching effect of exciton recombination. Fortunately, $CsPbBr_3$@glass exhibits excellent thermal reversibility after three-time heating/cooling cycles between 20 and 200 °C, with no significant

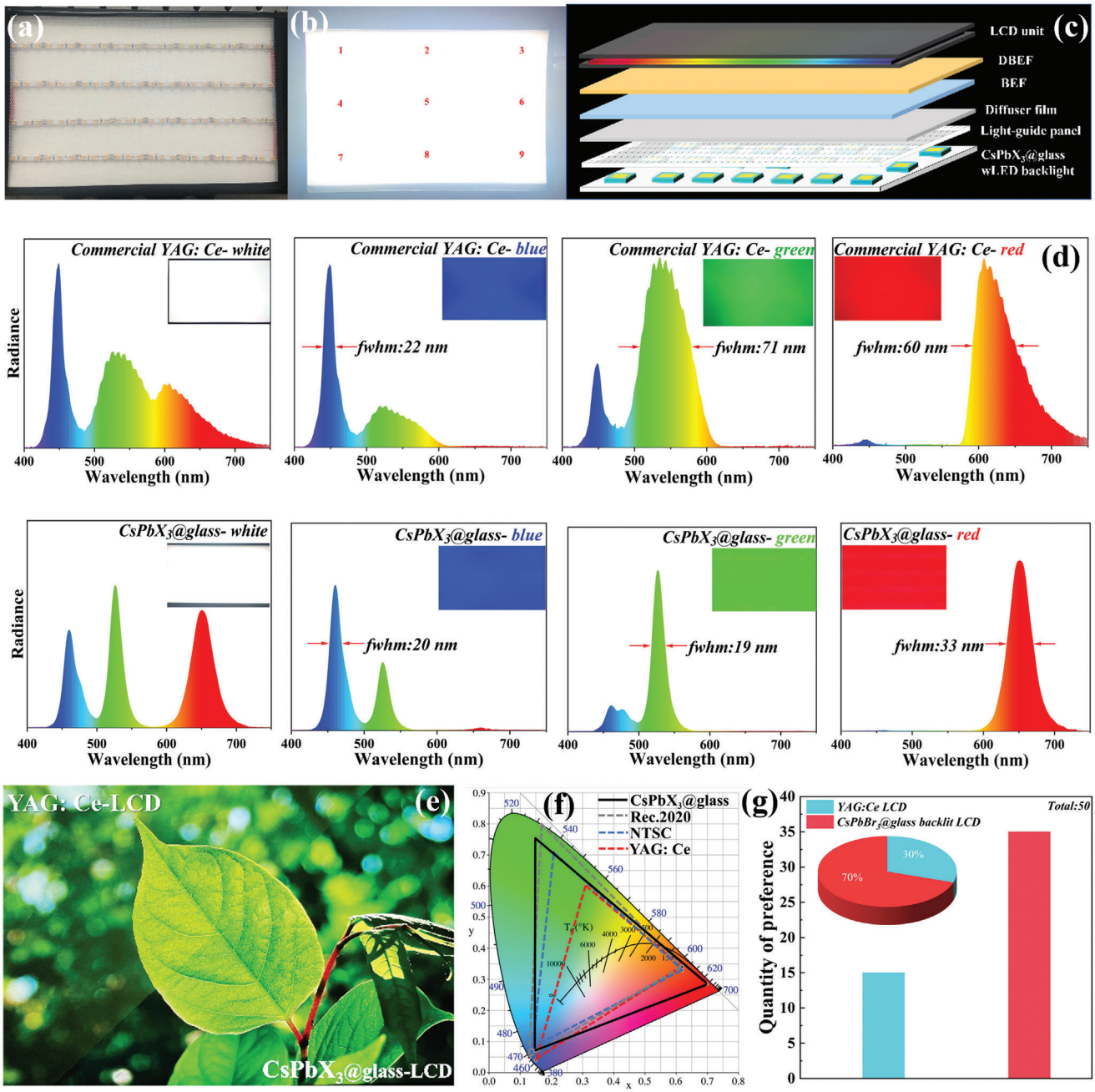

Figure 6. a) Photographs of $CsPbX_3$@glass-based wLED array and b) luminescent image of light guide panel under an operating voltage of 12 V. c) Schematic structure of the $CsPbX_3$@glass-based backlit LCD device. BEF and DBEF represent brightness enhancement film and dual brightness enhancement film, respectively. d) PL radiance spectra of white, blue, green, and red images directly recorded from commercial LCD screen and $CsPbX_3$@glass-based LCD screen via a luminance meter. e) Comparison of display from LCD screens with commercial YAG: Ce-converted wLED backlit unit and $CsPbX_3$@glass-based one. f) Color gamut of $CsPbX_3$@glass-based LCD (black solid triangle), Rec.2020 standard (grey dot triangle), NSTC 1953 standard (blue dash triangle), and commercial backlit LCD (red dot triangle). g) Statistics on the number of preferences for the two kinds of LCDs. Inset is pie chart for percentage of people.

change in PL intensity (**Figure 5**a; Figure S11, Supporting Information). In addition, the $CsPbBr_3$@glass samples exhibit superior resistance to moisture and heat, owing to the protection of a robust glass network that effectively isolates $CsPbBr_3$ PeQDs from the external environment. After 1000 h of accelerated aging test with commercial standard of 85 °C/85% RH, $CsPbBr_3$@glass can maintain 92% of the initial PL intensity (Figure 5b). The contour plots of PL spectra versus time and the corresponding CIE color coordinates exhibit no obvious alteration, indicating a remarkable temperature and moisture resistance (Figure 5b,c; Table S5, Supporting Information). More importantly, the blue light irradiation stability of $CsPbBr_3$@glass

determines its potential as color converting material in blue-light-excited LED for display applications. Therefore, we tested photostability by placing $CsPbBr_3$@glass on a blue light guide panel with an optical power of 40 W m^{-2}. After >2000 h blue light irradiation, $CsPbBr_3$@glass can remain 84% of the initial PL intensity (Figure 5d). The corresponding contour plots and CIE color coordinates evidence that the sample is essentially exempt from exchanging halide anions and CIE color shifting under intensive blue light irradiation (Figure 5d,e; Table S5, Supporting Information). All the results verify that the protection of glass is sufficient to ensure long-term stability of $CsPbBr_3$ PeQDs for practical display application.

The excellent optical performance and stability of $CsPbBr_3$@glass provide a good basis for the implementation of direct downward backlit unit. First, we prepared red $CsPb(Br/I)_3$@glass with the emitting wavelength of 650 nm and IQE/EQE of 93%/72% (Experimental Section and Figure S12, Supporting Information). Second, we made a white LED (wLED) by coupling green 6-ZrO_2 $CsPbBr_3$@glass and red $CsPb(Br/I)_3$@glass powders with a 450 nm blue chip (Figure S13, Supporting Information). Finally, we achieved a white backlit unit by embedding equally spaced 96 $CsPbX_3$@glass wLED arrays in the light guide panel (**Figure 6**a). At a driven voltage/current of 12 V/1A, the backlit module can yield high-brightness and uniform white light (Figure 6b). The radiance spectra of nine points on the backlit module using a luminance meter were recorded, and apparently, each position has almost the same output intensity and a similar blue/green/red spectral profile (Figure S14, Supporting Information). In addition, the $CsPbX_3$@glass backlit unit is continuously lightened up to 24 h, and no significant color deviating and radiance weakening are found (Figure S15, Supporting Information), proving its superior operating stability. In further work, a prototype display device is constructed by combining $CsPbX_3$@glass wLED backlit module with commercial TFT-LCD panel (Figure 6c). The designed LCD device is compared with a commercial LCD (TFTMD089030, Japan Display Inc.) to demonstrate its wide-color-gamut feature. The white and blue/green/red tri-color images and the corresponding radiance PL spectra after passing through color filters are recorded (Figure 6d). Apparently, pure green and red images of $CsPbX_3$@glass-based display show more remarkable color rendition and higher color saturation, which is benefited from narrower fwhm values of $CsPbX_3$ PeQDs (19 and 33 nm) than those of commercial YAG: Ce phosphors (71 and 60 nm). The green leaf images taken from these two LCDs are displayed in Figure 6e. Indeed, the $CsPbX_3$@glass-based display is purer in green and has clearer details of object, while the commercial one has a faint yellowish tint. As a consequence, according to the calculated CIE color coordinates (Table S6, Supporting Information), the color gamut of the $CsPbX_3$@glass-based LCD reaches as high as 88% of Rec. 2020 standard and 118% of NTSC standard (Figure 6f), being far larger than that of the commercial YAG: Ce based LCD (68% of NTSC standard).

Finally, we conducted an anonymous personal preference vote of 50 people on two kinds of displays showing the same images (Figure 6e; Figure S16, Supporting Information). In this random test of 50 passers-by, 70% people preferred the bright green, fine details, and definition of the $CsPbX_3$@glass backlit LCD; while for the commercial YAG: Ce backlit display, the overall tone was considered to be warm yellow with a relative low contrast. The results of the poll certainly verify that high-color-purity $CsPbBr_3$@glass-based displays are more easily enjoyed by the public (Figure 6g; Table S7, Supporting Information).

3. Conclusion

In summary, we have successfully modulated the polymerization degree of the borosilicate glass network structure via the addition of ZrO_2. This will lead to well confined in situ nucleation/growth of $CsPbBr_3$ PeQDs inside glass rather than self-crystallization, which is conductive to the reduction of surface defects, the improvement of QD quality, and the promotion of radiative recombination of excitons. The present $CsPbB_3$@glass can yield green emission at 527 nm with high color purity of 88% and a record-high EQE of 75%, and the as-fabricated film can produce high luminance of 2647 cd m^{-2} upon blue light excitation (375 cd m^{-2}). Benefited from the effective isolation of PeQDs from external environment by a tight glass network, $CsPbBr_3$@glass maintains 92% and 85% of the initial PL after accelerated aging test (85 °C/85% RH) for 1000 h and high-power blue light (40 W m^{-2}) irradiation >2000 h, respectively. In the end, we designed a straight-down backlit module using $CsPbBr_3$@glass as color converter to emit stable and uniform white light, which enables the constructed prototype LCD device to display images with wide color gamut of 118% NTSC standard and more realistic color rendition of objects. This work will motivate future investigation on finely regulating microstructure and optical performance of PeQDs@glass composites for practical application in backlit display.

Supporting Information

Supporting Information is available from the Wiley Online Library or from the author.

Acknowledgements

This work was supported by the National Key Research and Development Program of China (2021YFB3500503), the National Natural Science Foundation of China (52272141, 51972060, 12074068, 52102159, and 22103013), the Fujian Science & Technology Innovation Laboratory for Optoelectronic Information (2021ZZ126), the Natural Science Foundation of Fujian Province (2020J02017, 2022J05091, 22021J06021, 2021J01190, 2020J01931, and 2020H0026), and the Organic Optoelectronics Engineering Research Center of Fujian's Universities, Fujian Jiangxia University (grant no. JXKFA202201).

Conflict of Interest

The authors declare no conflict of interest.

Data Availability Statement

Research data are not shared.

Keywords

composites, glasses, light-emitting diodes, luminescent materials, perovskite quantum dots

Received: August 7, 2023
Revised: September 19, 2023
Published online:

[1] Y. Shu, X. Lin, H. Qin, Z. Hu, Y. Jin, X. Peng, *Angew. Chem., Int. Ed.* **2020**, *59*, 22312.
[2] H.-W. Chen, R.-D. Zhu, J. He, W. Duan, W. Hu, Y.-Q. Lu, M.-C. Li, S.-L. Lee, Y.-J. Dong, S.-T. Wu, *Light: Sci. Appl.* **2017**, *6*, 17043.
[3] R. Zhang, H. Lin, Y. Yu, D. Chen, J. Xu, Y. Wang, *Laser Photonics Rev.* **2014**, *8*, 158.
[4] X. Wang, Z. Bao, Y.-C. Chang, R.-S. Liu, *ACS Energy Lett.* **2020**, *5*, 3374.
[5] S. Liao, Z. Yang, J. Lin, S. Wang, J. Zhu, S. Chen, F. Huang, Y. Zheng, D. Chen, *Adv. Funct. Mater.* **2023**, *33*, 2210558.
[6] C. Otero-Martínez, J. Ye, J. Sung, I. Pastoriza-Santos, J. Pérez-Juste, Z. Xia, A. Rao, R. L. Z. Hoye, L. Polavarapu, *Adv. Mater.* **2022**, *34*, 2107105.
[7] C. Wei, W. Su, J. Li, B. Xu, Q. Shan, Y. Wu, F. Zhang, M. Luo, H. Xiang, Z. Cui, H. Zeng, *Adv. Mater.* **2022**, *34*, 2107798.
[8] Q. A. Akkerman, T. P. T. Nguyen, S. C. Boehme, F. Montanarella, D. N. Dirin, P. Wechsler, F. Beiglböck, G. Rainò, R. Erni, C. Katan, J. Even, M. V. Kovalenko, *Science* **2022**, *377*, 1406.
[9] Y. Jiang, C. Sun, J. Xu, S. Li, M. Cui, X. Fu, Y. Liu, Y. Liu, H. Wan, K. Wei, T. Zhou, W. Zhang, Y. Yang, J. Yang, C. Qin, S. Gao, J. Pan, Y. Liu, S. Hoogland, E. H. Sargent, J. Chen, M. Yuan, *Nature* **2022**, *612*, 679.
[10] C.-Y. Huang, H. Li, Y. Wu, C.-H. Lin, X. Guan, L. Hu, J. Kim, X. Zhu, H. Zeng, T. Wu, *Nano-Micro Lett.* **2022**, *15*, 16.
[11] T.-H. Han, K. Y. Jang, Y. Dong, R. H. Friend, E. H. Sargent, T.-W. Lee, *Nat. Rev. Mater.* **2022**, *7*, 757.
[12] M. He, Q. Zhang, F. Carulli, A. Erroi, W. Wei, L. Kong, C. Yuan, Q. Wan, M. Liu, X. Liao, W. Zhan, L. Han, X. Guo, S. Brovelli, L. Li, *ACS Energy Lett.* **2023**, *8*, 151.
[13] R. K. Singh, L.-H. Chen, A. Singh, N. Jain, J. Singh, C.-H. Lu, *Front. Nanotechnol.* **2022**, *4*, 863312.
[14] Z. Luo, D. Xu, S.-T. Wu, *J. Disp. Technol.* **2014**, *10*, 526.
[15] H. Chen, J. He, S. T. Wu, *IEEE J. Sel. Top. Quantum Electron.* **2017**, *23*, 1900611.
[16] H. L. Ji, S. J. Cheng, P. F. Li, Y. Zhang, Z. Y. Ge, H. Z. Zhong, *Chin. Opt.* **2022**, *15*, 132.
[17] K. Hills-Kimball, H. Yang, T. Cai, J. Wang, O. Chen, *Adv. Sci.* **2021**, *8*, 2100214.
[18] Y. Bai, M. Hao, S. Ding, P. Chen, L. Wang, *Adv. Mater.* **2022**, *34*, 2105958.
[19] A. Ghorai, S. Mahato, S. Singh, S. Bose, B. Roy, U. Jeong, S. Kumar Ray, *Angew. Chem., Int. Ed.* **2023**, *62*, 202302852.
[20] B. Ai, C. Liu, J. Wang, J. Xie, J. Han, X. Zhao, *J. Am. Ceram. Soc.* **2016**, *99*, 2875.
[21] S. Yuan, D. Chen, X. Li, J. Zhong, X. Xu, *ACS Appl. Mater. Interfaces* **2018**, *10*, 18918.
[22] Y. Ye, W. Zhang, Z. Zhao, J. Wang, C. Liu, Z. Deng, X. Zhao, J. Han, *Adv. Opt. Mater.* **2019**, *7*, 1801663.
[23] X. Huang, Q. Guo, D. Yang, X. Xiao, X. Liu, Z. Xia, F. Fan, J. Qiu, G. Dong, *Nat. Photonics* **2020**, *14*, 82.
[24] J. Lin, Y. Lu, X. Li, F. Huang, C. Yang, M. Liu, N. Jiang, D. Chen, *ACS Energy Lett.* **2021**, *6*, 519.
[25] X. Liu, E. Mei, Z. Liu, J. Du, X. Liang, W. Xiang, *ACS Photonics* **2021**, *8*, 887.
[26] K. Sun, D. Tan, X. Fang, X. Xia, D. Lin, J. Song, Y. Lin, Z. Liu, M. Gu, Y. Yue, J. Qiu, *Science* **2022**, *375*, 307.
[27] J. Li, Y. Fan, T. Xuan, H. Zhang, W. Li, C. Hu, J. Zhuang, R.-S. Liu, B. Lei, Y. Liu, X. Zhang, *ACS Appl. Mater. Interfaces* **2022**, *14*, 30029.
[28] B. Yang, S. Mei, Y. Zhu, D. Yang, H. He, R. Hu, Y. Li, J. Zou, R. Guo, *Ceram. Int.* **2023**, *49*, 6720.
[29] C. Yang, B. Zhuang, J. Lin, S. Wang, M. Liu, N. Jiang, D. Chen, *Chem. Eng. J.* **2020**, *398*, 125616.
[30] D. Wang, J. Qiu, D. Zhou, S. Hu, Y. Wen, K. Zhang, Q. Wang, Y. Yang, H. Wu, Z. Long, X. Li, J. Pi, E. Cao, *Chem. Eng. J.* **2021**, *421*, 127777.
[31] Z. Yang, H. Zhang, Z. Fang, J. Yi, P. Song, X. Yu, D. Zhou, J. Qiu, X. Xu, *Chem. Eng. J.* **2022**, *427*, 131379.
[32] K. Sun, D. Tan, J. Song, W. Xiang, B. Xu, J. Qiu, *Adv. Opt. Mater.* **2021**, *9*, 2100094.
[33] C. Li, M. Li, *J. Raman Spectrosc.* **2002**, *33*, 301.
[34] A. Grandjean, M. Malki, V. Montouillout, F. Debruycker, D. Massiot, *J. Non-Cryst. Solids* **2008**, *354*, 1664.
[35] X. Zhang, L. Hu, J. Ren, *J. Phys. Chem. C* **2020**, *124*, 8919.
[36] N. Bisbrouck, M. Bertani, F. Angeli, T. Charpentier, D. De Ligny, J.-M. Delaye, S. Gin, M. Micoulaut, *J. Am. Ceram. Soc.* **2021**, *104*, 4518.
[37] L. Zhu, M. Wang, Y. Xu, X. Zhang, P. Lu, *J. Am. Ceram. Soc.* **2022**, *105*, 5698.
[38] V. G. Antunes, C. A. Figueroa, F. Alvarez, *Appl. Surf. Sci.* **2018**, *448*, 502.
[39] M. Tashiro, S. Sukenaga, S. Kawanishi, Y. Sato, Y. Takakuwa, H. Shibata, *J. Am. Ceram. Soc.* **2020**, *103*, 5139.
[40] S. Damyanova, P. Grange, B. Delmon, *J. Catal.* **1997**, *168*, 421.
[41] T. V. Larina, L. S. Dovlitova, V. V. Kaichev, V. V. Malakhov, T. S. Glazneva, E. A. Paukshtis, B. S. Bal'zhinimaev, *RSC Adv.* **2015**, *5*, 79898.
[42] C. Thunyaratchatanon, A. Luengnaruemitchai, T. Chaisuwan, N. Chollacoop, S.-Y. Chen, Y. Yoshimura, *Microporous Mesoporous Mater.* **2017**, *253*, 18.
[43] P. Satyanarayana, A. V. Deshpande, *J. Solid State Chem.* **2022**, *316*, 123600.
[44] D. Chen, Y. Liu, C. Yang, J. Zhong, S. Zhou, J. Chen, H. Huang, *Nanoscale* **2019**, *11*, 17216.
[45] S. Chen, J. Lin, S. Zheng, Y. Zheng, D. Chen, *Adv. Funct. Mater.* **2023**, *33*, 2213442.